Computers and Geotechnics 148 (2022) 104841

Contents lists available at ScienceDirect

Computers and Geotechnics

journal homepage: www.elsevier.com/locate/compgeo

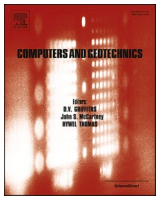

Translational upper bound limit analysis of shallow landslides accounting for pore pressure effects

Wengui Huang [a,*], Fleur Loveridge [a], Alfrendo Satyanaga [b]

[a] School of Civil Engineering, University of Leeds, Leeds, UK
[b] Department of Civil and Environmental Engineering, Nazarbayev University, Nur-Sultan, Kazakhstan

ARTICLE INFO

Keywords:
Slope stability
Shallow landslide
Upper bound limit analysis
Infinite slope model
Boundary effect

ABSTRACT

Many rainfall-induced landslides are reported to be shallow. Therefore, when regional slope stability analysis, or landslide hazard mapping is carried out, simple approaches, such as the infinite slope model, are often used. However, the infinite slope model is known to underestimate the factor of safety due to the absence of boundary effects. More sophisticated methods that account for the boundary effects at the toe and head of the landslide are much more computationally expensive. In this paper upper bound limit analysis (UBLA) is presented with a novel failure mechanism which consists of a translational parallelogram in the middle slope and two log-spiral components at the slope crest and slope toe to capture the boundary effect. The new approach is derived for a full range of pore water pressure conditions and validated by finite element limit analyses. For shallow landslides the translational UBLA is found to outperform the conventional log-spiral UBLA. The results of a large parametric study using the translational UBLA are then used to develop a novel analytical shallow landslide model which retains the simplicity of the traditional infinite slope model, but yet improves accuracy considerably, making this an attractive alternative for routine analysis such as landslide hazard mapping.

1. Introduction

Many rainfall-induced landslides are reported to be shallow with a depth commonly less than two meters (Perry, 1989; Kayyal and Wright, 1991; Dai et al., 2003; Dahal et al., 2009). Reduction in slope stability due to rainfall is mainly attributed to the redistribution of pore-water pressure (PWP) above the wetting front (Rahardjo et al. 1995). Typical PWP profiles in a soil slope are shown in Fig. 1. Before rainfall infiltration, PWP is negative above the water table, which increases the soil strength and contributes to stability (Fredlund and Rahardjo, 1993). Possible PWP redistributions under rainfall infiltration are shown as Profiles *a*, *b* and *c* in Fig. 1. Profile *a* represents the situation where negative water pressure is partially eliminated, Profile *b* completely eliminated, and positive water pressure is built up in Profile *c*. The three idealised PWP profiles cover most of the probable scenarios that a slope may experience under a rainfall. Numerical analyses have shown that PWP Profile *a* tends to occur in fine-grained soils, and PWP Profile *b* tends to occur in coarse-grained soils (Zhang et al., 2004; Lee et al., 2009). PWP Profile *c* tends to occur in layered soils where a permeable layer is underlain by a less permeable layer (Cho, 2009).

The infinite slope model is a classical stability method for the analysis of shallow landslides (Taylor, 1948). It assumes that failure takes place along a plane, which is parallel to the slope surface, and that the boundary effects at the two ends are negligible. Because of these underlying assumptions, the factor of safety can be calculated explicitly (i.e., without iteration) as a function of soil properties, pore-water pressure and sliding depth (e.g., Rahardjo et al. 1995). The analytical nature of the infinite slope model makes it well suited for regional stability analyses (e.g., landslide hazard mapping) (e.g., Iverson, 2000; Harp et al. 2006; Baum et al. 2008; Park et al. 2013; Chen & Zhang, 2014). However, due to the absence of boundary effects, the infinite slope model is only accurate when the depth of the failure mass is much less than its length (Taylor, 1948). It can increasingly underestimate the factor of safety by up to 100% with the increase in depth/length ratio of the landslide (Griffiths et al. 2011; Milledge et al. 2012). The funding available for slope maintenance and hazard prevention is often limited and constrained by the financial environment (Huang, 2021). Therefore, it is important to have high accuracy regional slope stability analyses in order to correctly identify the critical slopes that require the most urgent attention.

Shallow landslides can also be analysed by adapting the limit equilibrium method (LEM) of slices (Lian and Wu, 2021) or by strength

* Corresponding author.
E-mail address: W.Huang@leeds.ac.uk (W. Huang).

https://doi.org/10.1016/j.compgeo.2022.104841
Received 11 February 2022; Received in revised form 3 May 2022; Accepted 23 May 2022
Available online 2 June 2022

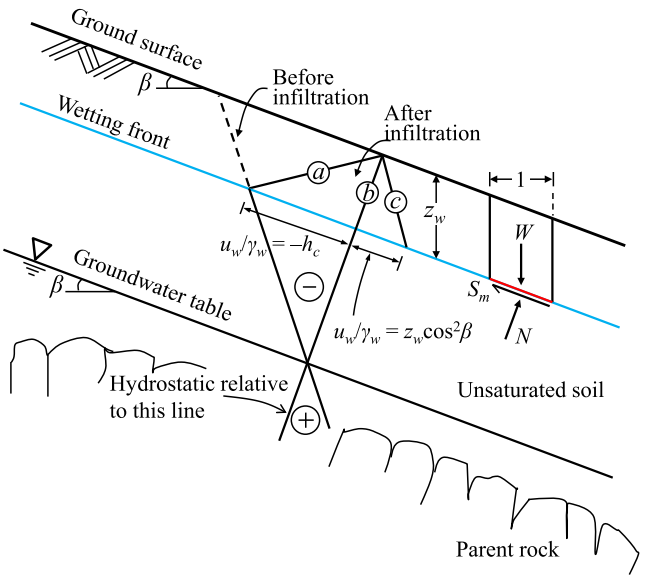

Fig. 1. Possible pore-water pressure profiles (***a***, ***b***, and ***c***) in an unsaturated slope under rainfall (modified from Rahardjo et al. 1995).

reduction finite element method (FEM) (Griffiths et al. 2011; Milledge et al. 2012; Huang et al. 2015). Both LEM and FEM can consider boundary effects, hence they provide more accurate stability assessment than infinite slope analysis. However, due to the computational expense required by LEM and FEM, they are generally reserved for site-specific analysis and not for regional stability analyses.

The main criticism of LEM lies in the prior assumptions that are required regarding interslice forces (e.g., Michalowski, 1995). This can be avoided by utilising FEM; however, the accuracy is mesh dependent. This mesh dependency is particularly pertinent for shallow landslide problems, as meshing of a long thin slide is challenging. The challenge is greater with the decrease in depth/length ratio (Huang et al. 2015). Among traditional stability analysis methods, analytical upper bound limit analysis (UBLA) is the method that is free from both interslice force assumptions and mesh dependency (Sloan, 2013). The effectiveness of UBLA with a log-spiral failure mechanism for homogeneous slopes has been widely proven (Chen, 1975; Michalowski, 1995). However, for a shallow translational landslide, a significant portion of the slip surface is a plane parallel to the slope surface (e.g., Fig. 1). This is a considerable deviation from the logarithmic spiral assumption. Therefore, the log-spiral failure mechanism may not be the most effective failure mechanism for the analysis of shallow translational landslides. A hybrid translational mechanism accounting for boundary effects that is more suitable for shallow landslides has been proposed (Huang et al., 2018). Yet, this remains to be tested more widely, including for the full range of PWP profiles shown in Fig. 1.

In this study, application of UBLA to conventional infinite slope problems and the novel hybrid translational mechanism of Huang et al (2018) is presented, before these are extended to the full range of PWP conditions in Fig. 1 (Section 2). Finite element limit analyses (both lower and upper bounds) are then used to validate the translational UBLA, before this is used to explore the influence of PWP effects on the shape of the failure surface (Section 3 & 4). Results of a large parametric study using the validated translational UBLA are subsequently used to develop a new analytical shallow landslide model that is as simple to apply as the traditional infinite slope model, yet offers much greater accuracy due to the inclusion of boundary effects (Section 5).

2. Upper bound limit analysis (UBLA) of shallow landslides

The likely PWP redistributions in a soil slope under rainfall are shown as Profiles *a*, *b* and *c* in Fig. 1. The PWP for the various profiles can be mathematically expressed as:

$$u_w(z) = \begin{cases} -\dfrac{z}{z_w}\gamma_w h_c & \text{for Profile } (a) \\ 0 & \text{for Profile } (b) \\ \gamma_w z(\cos\beta)^2 & \text{for Profile } (c) \end{cases} \quad (1)$$

where z_w denotes the depth of wetting front, u_w denotes the PWP at a vertical depth of z ($0 \le z \le z_w$), γ_w denotes the unit weight of water, h_c denotes the initial suction head at $z = z_w$ before rainfall infiltration, and β denotes the slope angle. PWP effects are first incorporated into the infinite slope UBLA, and then to the hybrid translational UBLA.

2.1. Infinite slope UBLA

Infinite slope analysis can be conducted on a representative vertical slice of unit width, as shown in Fig. 2. UBLA involves the construction of a kinematically admissible velocity field and establishing the work-rate balance equation. To be kinematically admissible, the velocity jump vector $\boldsymbol{v}$ at the slip surface is inclined to the slip surface with an angle equals to the effective angle of internal friction ϕ' (i.e., dilation angle = ϕ') (Chen, 1975; Davis & Selvadurai, 2002). The rate of work done by the soil weight $\dot{W}_\gamma$ can be calculated as:

$$\dot{W}_\gamma = \int_A \boldsymbol{\gamma} \bullet \boldsymbol{v} \mathrm{d}A = \gamma z_w v \sin(\beta - \phi') \quad (2)$$

where A denotes the cross-sectional area ($= z_w \times 1$), $\boldsymbol{\gamma}$ is the unit weight vector.

The rate of work done by water pressure $\dot{W}_{u_w}$ can be calculated as (Michalowski, 1995; Huang, 2018):

$$\dot{W}_{u_w} = \int_S \chi u_w v_n \mathrm{d}S = \chi u_w v \frac{\sin\phi'}{\cos\beta} \quad (3)$$

where S denotes the slip surface, v_n denotes the normal component of the velocity jump vector, and χ is the effective stress parameter defined by Bishop & Bright (1963). There is some debate on the effective stress concept in unsaturated soils (e.g. Nuth & Laloui, 2008). Bishop's single effective stress approach is adopted here, as it offers advantages for the transition between saturated and unsaturated soils, and it is appropriate for stability related problem where strength is the main interest (Nuth & Laloui, 2008).

The energy dissipation for Mohr-Coulomb materials, $\dot{D}$ can be calculated as (Chen, 1975; Davis & Selvadurai, 2002):

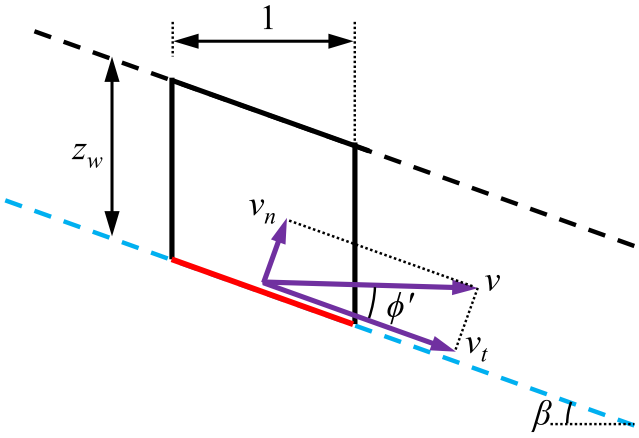

Fig. 2. Upper bound limit analysis of an infinite slope.

$$\dot{D} = \int_S c' v_t \mathrm{d}S = c' v \frac{\cos\phi'}{\cos\beta} \tag{4}$$

where c' is effective cohesion of the soil, v_t denotes the tangential component of the velocity jump vector.

Equating the rate of work to energy dissipation gives:

$$\gamma z_w \left[\sin\beta\cos\beta - (\cos\beta)^2 \tan\phi'\right] v \frac{\cos\phi'}{\cos\beta} + \chi u_w \tan\phi' v \frac{\cos\phi'}{\cos\beta} = c' v \frac{\cos\phi'}{\cos\beta} \tag{5}$$

At limit state, in Eq. (5) the parameter c' is more clearly denoted as c'_m ($= \frac{c'}{F}$) and ϕ' as ϕ'_m ($\tan\phi'_m = \frac{\tan\phi'}{F}$). By cancelling $v\frac{\cos\phi'}{\cos\beta}$ in the left and right-hand-side, Eq. (5) can be rearranged as:

$$F = \frac{c'}{\gamma z_w \sin\beta\cos\beta} + \frac{\tan\phi'}{\tan\beta} - \frac{\chi u_w \tan\phi'}{\gamma z_w \sin\beta\cos\beta} \tag{6}$$

Equation (6) is the general expression of factor of safety for the various PWP profiles shown in Fig. 1, and u_w is calculated by Eq. (1) with $z = z_w$. The effective stress parameter $\chi = 1$ for saturated slopes. For unsaturated soils, $0 \le \chi \le 1$, the parameter χ can be inferred from the soil–water retention curve or simply approximated as degree of saturation (Bishop & Bright, 1963). As it is derived from UBLA, Eq. (6) gives upper bound solution.

The infinite slope model is commonly derived through stress equilibrium (e.g., Taylor, 1948; Rahardjo et al., 1995), as indicated in Fig. 1, taking a slice of unit width, and leads to the same expression as Eq. (6). Hence, Eq. (6) is also a lower bound solution (Atkinson, 2007). An exact solution is usually not available for slope stability problem (Yu et al. 1998). The coincidence of upper and lower bound solutions means that Eq. (6) gives the exact solutions for infinite slopes. It also reveals that the associated flow rule assumption (i.e., dilation angle = ϕ') does not compromise the accuracy of the UBLA, at least for the infinite slope problem.

2.2. Translational UBLA

The log-spiral failure has been proven to be the most effective failure mechanism for simple homogeneous slopes among all the kinematically admissible failure modes (Chen, 1975). As illustrated in Fig. 3, the log-spiral slip surface is defined by:

$$r(\theta) = r_o e^{(\theta-\theta_o)\tan\phi'} \tag{7}$$

where $r(\theta)$ is the radius of the log-spiral at angle θ, e is the base of the natural logarithm (≈ 2.718), r_o is the initial radius, θ_o and θ_h are the initial and final angles of the log-spiral, respectively.

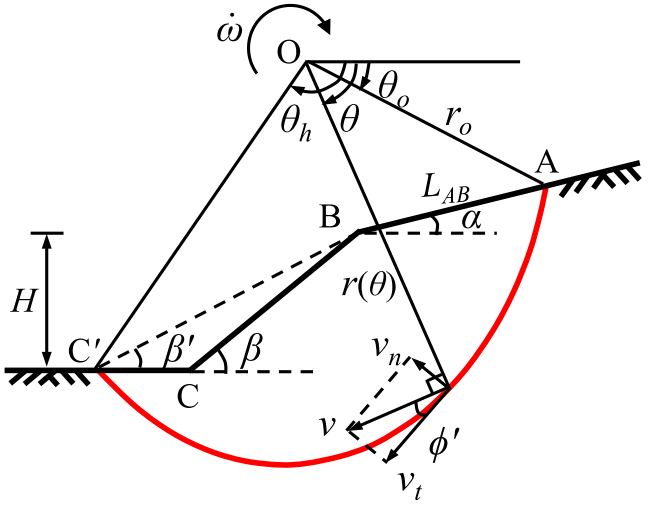

Fig. 3. Log-spiral failure mechanism (modified from Chen 1975).

The log-spiral failure mechanism is widely adopted in upper bound limit analysis (e.g., Chen, 1975; Michalowski, 1995; Qin and Chian, 2018; Ji et al. 2021). However, for shallow slope failures, which are commonly triggered by rainfall, the log-spiral failure mechanism may not lead to the most critical stability solution for cohesive-frictional slopes (Huang et al., 2016, 2018). Huang et al. (2018) proposed a kinematically admissible hybrid translational failure mechanism, as shown in Fig. 4. The failure mechanism consists of a main translational component in the middle slope (parallelogram DEFG) and two log-spiral components at the slope crest (ABDE) and slope toe (CFG) to capture boundary effects. To ensure a continuous velocity field and smooth transitions between the translational and rotational components, the log-spiral segments AE and CF are tangent to the sliding plane EF at points E and F, respectively. The velocity jump vector at the slip surface is inclined to the slip surface with an angle ϕ' to fulfil the requirement of kinematic admissibility. The velocity vectors at the interfaces DE and GF are indicated as arrows in Fig. 4(a). The vertical height of the translational component H_{trl} is variable and needs to be optimised to determine the most critical stability solution. When $H_{\mathrm{trl}} = 0$, the translational UBLA would reduce to the conventional log-spiral UBLA, as illustrated in Fig. 3 and Fig. 4(b).

For shallow slope stability problems, the translational UBLA can give a lower (more appropriate) factor of safety compared with the log-spiral UBLA, which may overestimate the result. The limitation of the previous study by Huang et al. (2018) is that it only applies to the situation where the PWP is zero above the wetting front (i.e., Profile *b* in Fig. 1). However, under rainfall positive PWP can be built-up (Profile *c*) in many field conditions (e.g., Zhan et al. 2007; Smethurst et al. 2012) or occasionally suction (Profile *a*) can be partially maintained (e.g., Rahardjo et al. 1995). A significant improvement is made in this study by extending the analysis by Huang et al. (2018) to consider both positive and negative PWP effects.

2.2.1. PWP Profile b ($u_w = 0$)

In the translational UBLA, the log-spiral components at the slope crest and slope toe are combined into a single rotational component, as shown in Fig. 4(b). The work rate for the translational component (DEFG in Fig. 4a) and the combined rotational component (Fig. 4b) are derived separately. The vertical height of the translational component H_{trl} and the combined rotational component H_{rot} satisfy:

$$H_{\mathrm{trl}} + H_{\mathrm{rot}} = H \tag{8}$$

where H is the height of the slope. In Eq. (8) and the rest of this paper, the subscript (or superscript) "trl" denotes "translational" and "rot" denotes "rotational".

Translational UBLA with Profile *b* is presented by Huang et al. (2018). The analysis for Profile *b* is briefly recapped here, on which the analysis for Profile *a* and Profile *c* will be further developed. According to Eq. (1b), $u_w = 0$ for Profile *b*, which leads to $\dot{W}_{u_w} = 0$. Hence, the work rate balance equation can simply be written as:

$$\dot{W}_\gamma^{\mathrm{rot}} + \dot{W}_\gamma^{\mathrm{trl}} = \dot{D}_{c'}^{\mathrm{rot}} + \dot{D}_{c'}^{\mathrm{trl}} \tag{9}$$

where $\dot{W}_\gamma^{\mathrm{rot}}$ is the rate of work done by the weight of the rotational mass and calculated by:

$$\dot{W}_\gamma^{\mathrm{rot}} = \int_{A_{\mathrm{rot}}} \gamma . \mathbf{v} \mathrm{d}A_{\mathrm{rot}} = \dot{\omega}\gamma r_o^3 (f_1 - f_2 - f_3) \tag{10}$$

$\dot{W}_\gamma^{\mathrm{trl}}$ is the rate of work done by the weight of the translational mass and calculated by:

$$\dot{W}_\gamma^{\mathrm{trl}} = \int_{A_{\mathrm{trl}}} \gamma . \mathbf{v} \mathrm{d}A_{\mathrm{trl}} = \dot{\omega}\gamma r_o^3 f_\gamma^{\mathrm{trl}} \tag{11}$$

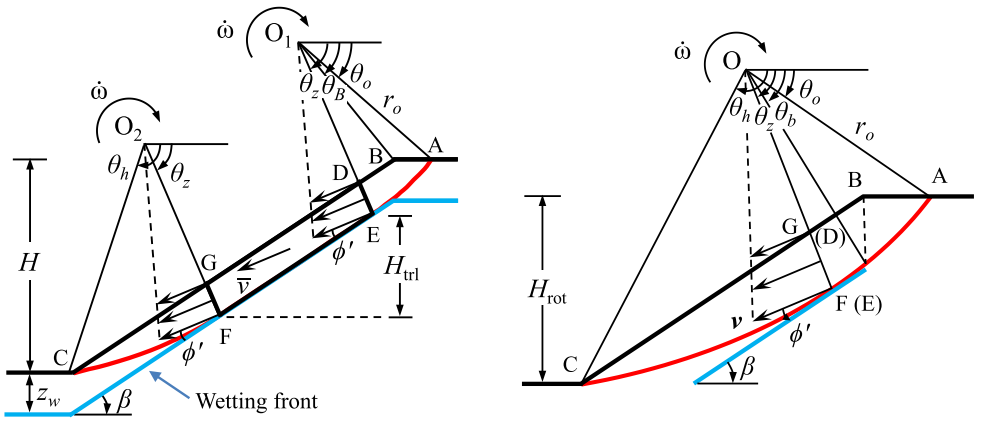

(a) Translational failure mechanism

(b) Combination of log-spiral components at slope crest (ABDE) and slope toe (CFG)

Fig. 4. Kinematically admissible translational failure mechanism.

$\dot{D}_{c'}^{\mathrm{rot}}$ is the energy dissipation caused by the rotational mass and calculated by:

$$\dot{D}_{c'}^{\mathrm{rot}} = \int_{S_{\mathrm{rot}}} c' v_t \mathrm{d}S_{\mathrm{rot}} = \dot{\omega}\gamma r_o^3 \frac{c'}{\gamma H \tan\phi'} f_{c'}^{\mathrm{rot}} \tag{12}$$

$\dot{D}_{c'}^{\mathrm{trl}}$ is the energy dissipation caused by the translational mass and calculated by:

$$\dot{D}_{c'}^{\mathrm{trl}} = \int_{S_{\mathrm{trl}}} c' v_t \mathrm{d}S_{\mathrm{trl}} = \dot{\omega}\gamma r_o^3 \frac{c'}{\gamma H \tan\phi'} f_{c'}^{\mathrm{trl}} \tag{13}$$

From Eq. (10) to Eq. (13), $\dot{\omega}$ denotes the rate of rotation, as shown in Fig. 4. In Eq. (10) and Eq. (11), A denotes the cross-sectional area of the failure mass, γ and $\mathbf{v}$ denote the unit weight vector and velocity vector, respectively. In Eq. (12) and (13), S denotes the slip surface, and v_t denotes tangential component of the velocity vector. The coefficients f_1, f_2, f_3, f_γ^{trl}, $f_{c'}^{\mathrm{rot}}$, and $f_{c'}^{\mathrm{trl}}$ are provided in Appendix.

2.2.2. PWP Profile a ($u_w < 0$) and PWP Profile c ($u_w > 0$)

This study significantly improves the original analysis of Huang et al. (2018) by taking into account the PWP effects. To incorporate PWP, the work rate balance equation Eq. (9) is modified to:

$$\dot{W}_{\gamma}^{\mathrm{rot}} + \dot{W}_{\gamma}^{\mathrm{trl}} + \dot{W}_{u_w}^{\mathrm{rot}} + \dot{W}_{u_w}^{\mathrm{trl}} = \dot{D}_{c'}^{\mathrm{rot}} + \dot{D}_{c'}^{\mathrm{trl}} \tag{14}$$

where $\dot{W}_{u_w}^{\mathrm{rot}}$ and $\dot{W}_{u_w}^{\mathrm{trl}}$ denote the rate of work done by PWPs in rotational and translational component, respectively. They can be calculated by substituting Eq. (1) into Eq. (3). The final form of $\dot{W}_{u_w}^{\mathrm{rot}}$ in Eq. (14) can be written as:

$$\dot{W}_{u_w}^{\mathrm{rot}} = \dot{\omega}\gamma r_o^3 f_{u_w}^{\mathrm{rot}} \tag{15}$$

where $f_{u_w}^{\mathrm{rot}}$ is a dimensionless coefficient.

For PWP Profile c, $f_{u_w}^{\mathrm{rot}}$ can be calculated by:

$$f_{u_w}^{\mathrm{rot}} = \frac{\gamma_w}{\gamma}\cos^2\beta\tan\phi' \left[\int_{\theta_o}^{\theta_b} \frac{g_{\mathrm{AB}}(\theta) - y_s(\theta)}{r_o} e^{2(\theta-\theta_o)\tan\phi'} \mathrm{d}\theta + \int_{\theta_b}^{\theta_h} \frac{g_{\mathrm{BC}}(\theta) - y_s(\theta)}{r_o} e^{2(\theta-\theta_o)\tan\phi'} \mathrm{d}\theta \right] \tag{16a}$$

For PWP Profile a, $f_{u_w}^{\mathrm{rot}}$ can be calculated by:

$$f_{u_w}^{\mathrm{rot}} = -\chi\frac{\gamma_w}{\gamma}\frac{h_c}{z_w}\tan\phi' \left[\int_{\theta_o}^{\theta_b} \frac{g_{\mathrm{AB}}(\theta) - y_s(\theta)}{r_o} e^{2(\theta-\theta_o)\tan\phi'} \mathrm{d}\theta + \int_{\theta_b}^{\theta_h} \frac{g_{\mathrm{BC}}(\theta) - y_s(\theta)}{r_o} e^{2(\theta-\theta_o)\tan\phi'} \mathrm{d}\theta \right] \tag{16b}$$

In Eq. (16a) and Eq. (16b), the angle θ_b is indicated in Fig. 4(b), $g_{\mathrm{AB}}(\theta)$ and $g_{\mathrm{BC}}(\theta)$ denote the vertical coordinates at slope crest (AB in Fig. 4) and slope surface (BC in Fig. 4), respectively; $y_s(\theta)$ represents the vertical coordinate at the slip surface. The differences $g_{\mathrm{AB}}(\theta) - y_s(\theta)$ and $g_{\mathrm{BC}}(\theta) - y_s(\theta)$ would give the vertical depths. The integration in Eq. (16a) and Eq. (16b) can be evaluated analytically by Eq. (17) and Eq. (18), respectively.

$$\int \frac{g_{\mathrm{AB}}(\theta) - y_s(\theta)}{r_o} e^{2(\theta-\theta_o)\tan\phi'} \mathrm{d}\theta = \left[\frac{H_{\mathrm{rot}}}{r_o}\left(1 - \frac{\tan\alpha}{\tan\beta}\right) + \frac{x_o}{r_o}\tan\alpha - \frac{y_o}{r_o}\right] \frac{e^{2(\theta-\theta_o)\tan\phi'}}{2\tan\phi'} + \left(\tan\alpha\frac{\sin\theta + 3\tan\phi'\cos\theta}{1+9\tan^2\phi'} + \frac{-\cos\theta + 3\tan\phi'\sin\theta}{1+9\tan^2\phi'}\right) e^{3(\theta-\theta_o)\tan\phi'} \tag{17}$$

$$\int \frac{g_{\mathrm{BC}}(\theta) - y_s(\theta)}{r_o} e^{2(\theta-\theta_o)\tan\phi'} \mathrm{d}\theta = \left(\frac{x_o}{r_o}\tan\beta - \frac{y_o}{r_o}\right) \frac{e^{2(\theta-\theta_o)\tan\phi'}}{2\tan\phi'} + \left(\tan\beta\frac{\sin\theta + 3\tan\phi'\cos\theta}{1+9\tan^2\phi'} + \frac{-\cos\theta + 3\tan\phi'\sin\theta}{1+9\tan^2\phi'}\right) e^{3(\theta-\theta_o)\tan\phi'} \tag{18}$$

The ratio $\frac{H_{rot}}{r_o}$ in Eq. (17) can be calculated by:

$$\frac{H_{rot}}{r_o} = \frac{\sin\beta}{\sin(\beta-\alpha)}\left[\sin(\theta_h+\alpha)e^{(\theta_h-\theta_o)\tan\phi'} - \sin(\theta_o+\alpha)\right] \tag{19}$$

The ratios $\frac{x_o}{r_o}$ and $\frac{y_o}{r_o}$ in Eq. (17) and Eq. (18) can be calculated by Eq. (20) and Eq. (21), respectively.

$$\frac{x_o}{r_o} = -e^{(\theta_h-\theta_o)\tan\phi'}\cos\theta_h \tag{20}$$

$$\frac{y_o}{r_o} = e^{(\theta_h-\theta_o)\tan\phi'}\sin\theta_h \tag{21}$$

The final form of $\dot{W}^{trl}_{u_w}$ in Eq. (14) can be written as:

$$\dot{W}^{trl}_{u_w} = \dot{\omega}\gamma r_o^3 f^{trl}_{u_w} \tag{22}$$

where $f^{trl}_{u_w}$ is a dimensionless coefficient.

For PWP Profile *c*, $f^{trl}_{u_w}$ can be calculated by:

$$f^{trl}_{u_w} = \frac{\gamma_w}{\gamma}\cos^2\beta\frac{z_s}{r_o}\frac{H_{trl}}{r_o}\frac{\sin\phi'}{\sin\beta}e^{(\theta_z-\theta_o)\tan\phi'} \tag{23a}$$

For PWP Profile *a*, $f^{trl}_{u_w}$ can be calculated by:

$$f^{trl}_{u_w} = -\chi\frac{\gamma_w}{\gamma}\frac{h_c}{z_w}\frac{z_s}{r_o}\frac{H_{trl}}{r_o}\frac{\sin\phi'}{\sin\beta}e^{(\theta_z-\theta_o)\tan\phi'} \tag{23b}$$

In Eqs. (23a) and (23b), z_s denotes the vertical distance between the top (DG) and bottom (EF) of the translational mass in Fig. 4(a) and is calculated by:

$$\frac{z_s}{r_o} = (\cos\theta_z\tan\beta+\sin\theta_z)e^{(\theta_z-\theta_o)\tan\phi'} - (\cos\theta_h\tan\beta+\sin\theta_h)e^{(\theta_h-\theta_o)\tan\phi'} \tag{24}$$

The angle θ_z in Eqs. (23a), (23b) and (24) is indicated in Fig. 4 and calculated by:

$$\theta_z = 90^\circ - \beta + \phi' \tag{25}$$

Finally, the work rate balance equation Eq. (14) can be rearranged to:

$$\frac{\gamma H}{c'} = \frac{f^{rot}_{c'} + f^{trl}_{c'}}{\left(f_1 - f_2 - f_3 + f^{trl}_{\gamma} + f^{rot}_{u_w} + f^{trl}_{u_w}\right)\tan\phi'} \tag{26a}$$

Minimum $\frac{\gamma H}{c'}$ can be obtained with θ_o, θ_h and $\frac{H_{trl}}{H}$ being the variables. For PWP Profiles *b* and *c*, the input parameters are α, β, ϕ' and $\frac{z_w}{H}$. For PWP Profile *a*, additional input parameters χ and $\frac{h_c}{H}$ are required. At limit state, c' in the objective function Eq. (26a) is more clearly denoted as c'_m ($=\frac{c'}{F}$), and ϕ' among the given conditions is denoted as ϕ'_m ($\tan\phi'_m = \frac{\tan\phi'}{F}$). Alternatively, Eq. (26a) can be rewritten as:

$$\frac{c'}{\gamma H\tan\phi'} = \frac{f_1 - f_2 - f_3 + f^{trl}_{\gamma} + f^{rot}_{u_w} + f^{trl}_{u_w}}{f^{rot}_{c'} + f^{trl}_{c'}} \tag{26b}$$

The advantage of Eq. (26b) over Eq. (26a) is that the parameter group $\frac{c'}{\gamma H\tan\phi'}$ is independent of factor of safety *F*:

$$\frac{c'_m}{\gamma H\tan\phi'_m} = \frac{c'/F}{\gamma H\tan\phi'/F} = \frac{c'}{\gamma H\tan\phi'} \tag{27}$$

Consequently, stability solutions can be conveniently presented as a chart format $\frac{F}{\tan\phi'}$ versus $\frac{c'}{\gamma H\tan\phi'}$ (e.g., Huang et al. 2018). For a specific slope stability problem with given c', γ, H and ϕ' etc., the parameter group $\frac{c'}{\gamma H\tan\phi'}$ is known while ϕ'_m is unknown. In this situation, an iterative procedure can be conducted to search for ϕ'_m which satisfies Eq. (27). Consequently, *F* is calculated as $\frac{\tan\phi'}{\tan\phi'_m}$.

To ensure the physical feasibility of the slip surface, the optimization

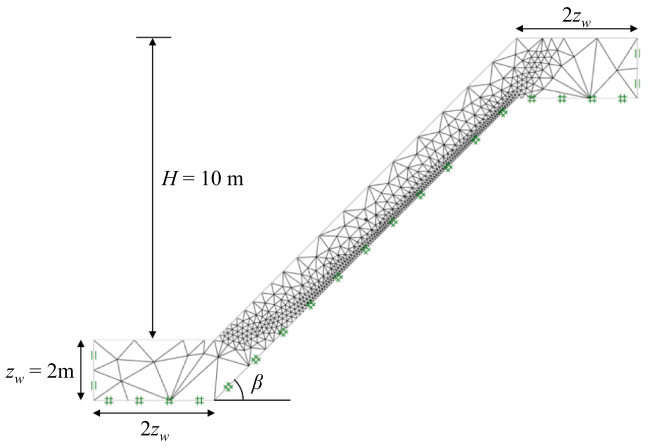

Fig. 5. Mesh and boundary conditions of the finite element model ($\beta = 45^\circ$).

for Eq. (26) is subjected to the following constraints: $0 \le \frac{H_{trl}}{H} < 1$, $z_s \le z_w$, $\phi' \le \theta_o \le \theta_B$, $\theta_B \le \theta_z$, and $\theta_z < \theta_h \le \pi + \phi' - \beta$. The angle θ_B is denoted in Fig. 4(a) and it can be calculated by:

$$\tan\theta_B = \frac{\sin\beta\sin(\theta_o+\alpha) - \sin\alpha\sin(\theta_h+\beta)e^{(\theta_h-\theta_o)\tan\phi'}}{-\cos\beta\sin(\theta_o+\alpha) + \cos\alpha\sin(\theta_h+\beta)e^{(\theta_h-\theta_o)\tan\phi'}} \tag{28}$$

3. Validation of the translational UBLA by finite element limit analysis

The effectiveness of the proposed translational UBLA is validated by finite element lower bound limit analysis (LBLA) and finite element UBLA. The finite element LBLA and finite element UBLA have been carried out using software OptumG2 (Krabbenhoft, 2019). In the comparison study, the slope geometry is $H = 10$ m, $z_w = 2$ m, $\beta = 18.4^\circ$, 26.6°, 33.7°, 45° or 63.4°. A typical finite element model is shown in

Table 1
Comparisons of factors of safety obtained by finite element lower bound limit analysis (LBLA), finite element upper bound limit analysis (UBLA), the proposed translational UBLA and the conventional log-spiral UBLA ($c' = 30$ kPa, $\phi' = 26^\circ$, $\gamma = 20$ kN/m^3, $H = 10$ m, $z_w = 2$. Additional parameters for Profiles *a* are: $\gamma_w h_c = 20$ kPa, $\chi = 1$).

PWP condition	β (°)	Factor of safety			
		Finite element LBLA	Finite element UBLA	Translational UBLA	Log-spiral UBLA
Profile *a* ($u_w < 0$)	18.4	5.502*	5.744*	5.570	6.031
	26.6	4.190*	4.351*	4.200	4.446
	33.7	3.594*	3.707*	3.584	3.755
	45.0	3.124*	3.264*	3.107	3.249
	63.4	3.233*	3.389*	3.245	3.495
Profile *b* ($u_w = 0$)	18.4	4.537	4.700	4.693	5.193
	26.6	3.421	3.541	3.533	3.812
	33.7	2.917	3.006	3.006	3.204
	45.0	2.499	2.603	2.586	2.748
	63.4	2.516	2.633	2.643	2.910
Profile *c* ($u_w > 0$)	18.4	3.785	3.959	3.915	4.453
	26.6	2.914	3.045	3.007	3.314
	33.7	2.524	2.620	2.611	2.830
	45.0	2.240	2.330	2.331	2.503
	63.4	2.375	2.498	2.525	2.795

(Note: * PWP Profile *a* cannot be modelled exactly by the software OptumG2. Hence, a constant value $u_w = -20$ kPa was assumed, which could slightly overestimate the factor of safety.).

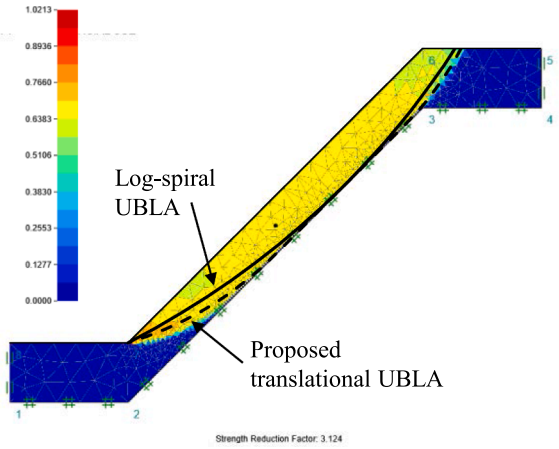

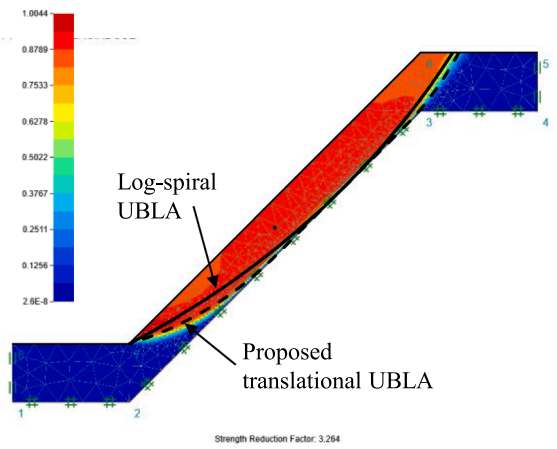

(a) Profile a ($u_w < 0$)

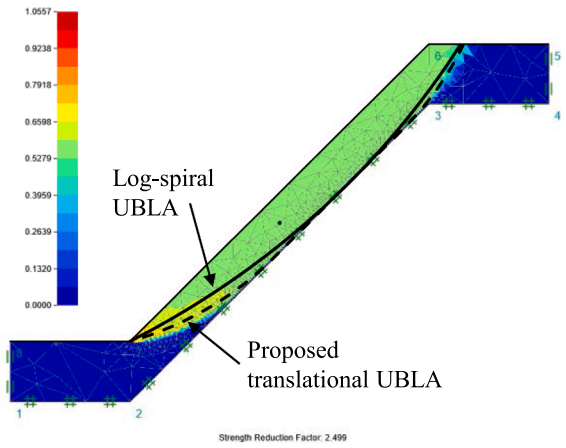

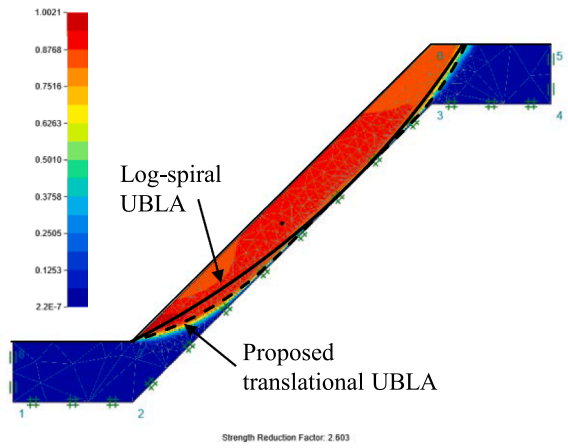

(b) Profile b ($u_w = 0$)

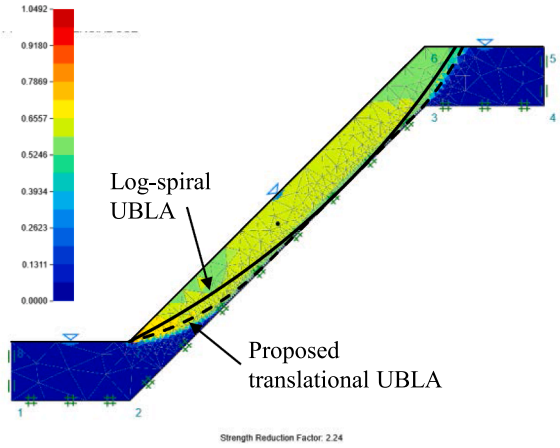

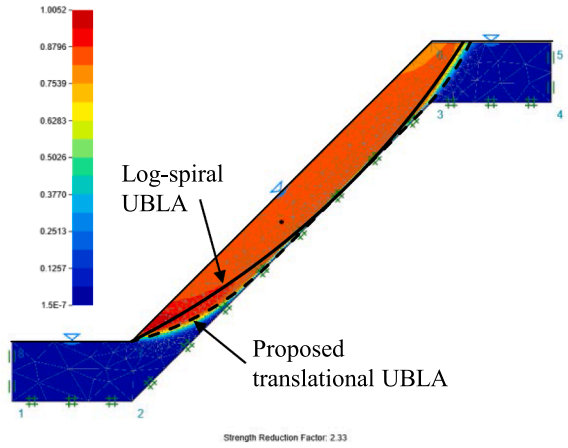

(c) Profile c ($u_w > 0$)

Fig. 6. Comparisons of failure mechanisms obtained by finite element lower bound limit analysis (LBLA) (left), finite element upper bound limit analysis (UBLA) (right), log-spiral UBLA (solid line) and the proposed translational UBLA (dashed line). ($\beta = 45°$, $c' = 30$ kPa, $\phi' = 26°$, $\gamma = 20$ kN/m^3, $H = 10$ m, $z_w = 2$ m. Additional parameters for Profiles a: $u_w = -20$ kPa, $\chi = 1$.).

Fig. 5 for $\beta = 45°$. In the OptumG2 modelling (version 2021 2.1.6), the number of element is set to 1000. The mesh adaptivity is enabled with 3 adaptive iterations, so that the mesh is automatically refined along the critical slip surface. The lengths of the left and right boundaries are twice of z_w (Griffiths et al. 2011; Huang et al. 2015). The bottom boundaries are fixed, while the left and right boundaries are only constrained in the horizontal direction. The soil parameters are $\gamma = 20$ kN/m^3, $c' = 30$ kPa, $\phi' = 26°$, which are typical residual soil properties for the Jurong Formation in Singapore reported by Rahardjo et al. (1995).

The residual soil of Jurong Formation can maintain a high degree of saturation for matric suctions up to 400 kPa (Rahardjo et al. 1995). For PWP Profile *a*, a small suction 20 kPa at the wetting front is adopted and $\chi = 1$ is well justified at this suction level.

The results from the finite element limit analyses are compared to the outputs from the proposed translational UBLA and the conventional log-spiral UBLA. The factors of safety obtained by different methods are summarised in Table 1, and comparisons of critical slip surfaces are shown in Fig. 6 for $\beta = 45°$. The critical slip surfaces obtained by the proposed translational UBLA are in good agreement with the finite element UBLA and in reasonable agreement with the finite element LBLA. The *F* obtained by the proposed translational UBLA are generally bracketed by the finite element LBLA and finite element UBLA. More specifically, the *F* by translational UBLA are closer to finite element UBLA for PWP Profiles *b* and *c*, and closer to finite element LBLA for PWP Profile *a*. It should be noted that PWP Profile *a* could not be modelled exactly by OptumG2, and a constant value $u_w = -20$ kPa was used. This assumption could overestimate the suction close to the boundary ($\widehat{AE}$ and $\widehat{CF}$ in Fig. 4a), therefore the *F* calculated by finite element LBLA and finite element UBLA for PWP Profile *a* could have been slightly overestimated. If PWP Profile *a* could be modelled exactly by OptumG2, the *F* calculated by finite element LBLA and finite element UBLA would be lower, and *F* obtained by translational UBLA would be closer to finite element UBLA.

The *F* obtained by the conventional log-spiral UBLA are, however, even greater than the finite element UBLA, and are therefore not safe for design purpose. The overprediction by the log-spiral UBLA is due to the fact that the assumed log-spiral fails to replicate the true slip surface which has a significant translational component, as shown in Fig. 6. The log-spiral UBLA also predicts a smaller failure volume compared to both finite element LBLA and finite element UBLA.

4. Influence of PWP effects on critical slip surfaces

The location of critical slip surface is known to be related to the dimensionless parameter group $\frac{c'}{\gamma H \tan\phi'}$ for both deep-seated rotational failure (Jiang and Yamagami, 2006) and shallow translational failure (Huang et al., 2018). Many rainfall-induced landslides are reported to be shallow. At the time when a failure occurs, the suction at the sliding surface may be partially retained, eliminated, or the water table may even be perched, as illustrated by PWP Profiles *a*, *b* and *c* in Fig. 1. An interesting question is whether the shape and location of the critical slip surface is also affected by the PWP condition for a shallow translational failure. To answer this question, a parametric study was carried out using the proposed translational UBLA. The effectiveness of the translational UBLA in replicating the true slip surface has been demonstrated in Fig. 6. In the parametric study, $\beta = 45°$, $H = 10$ m, $z_w = 2$ m, $\gamma = 20$ kN/m^3, $\phi' = 26°$, with c' ranges from 2 kPa to 30 kPa for PWP Profiles *b* and *c*, and additional parameters $\chi = 1$ and $u_w = -20$ kPa at the wetting front for PWP Profile *a*. The critical slip surfaces corresponding to the different PWP conditions and $\frac{c'}{\gamma H \tan\phi'}$ are summarised in Fig. 7. It is found that the location of the critical slip surface is rarely affected by PWP conditions and mainly determined by $\frac{c'}{\gamma H \tan\phi'}$. Fig. 7 also shows that the

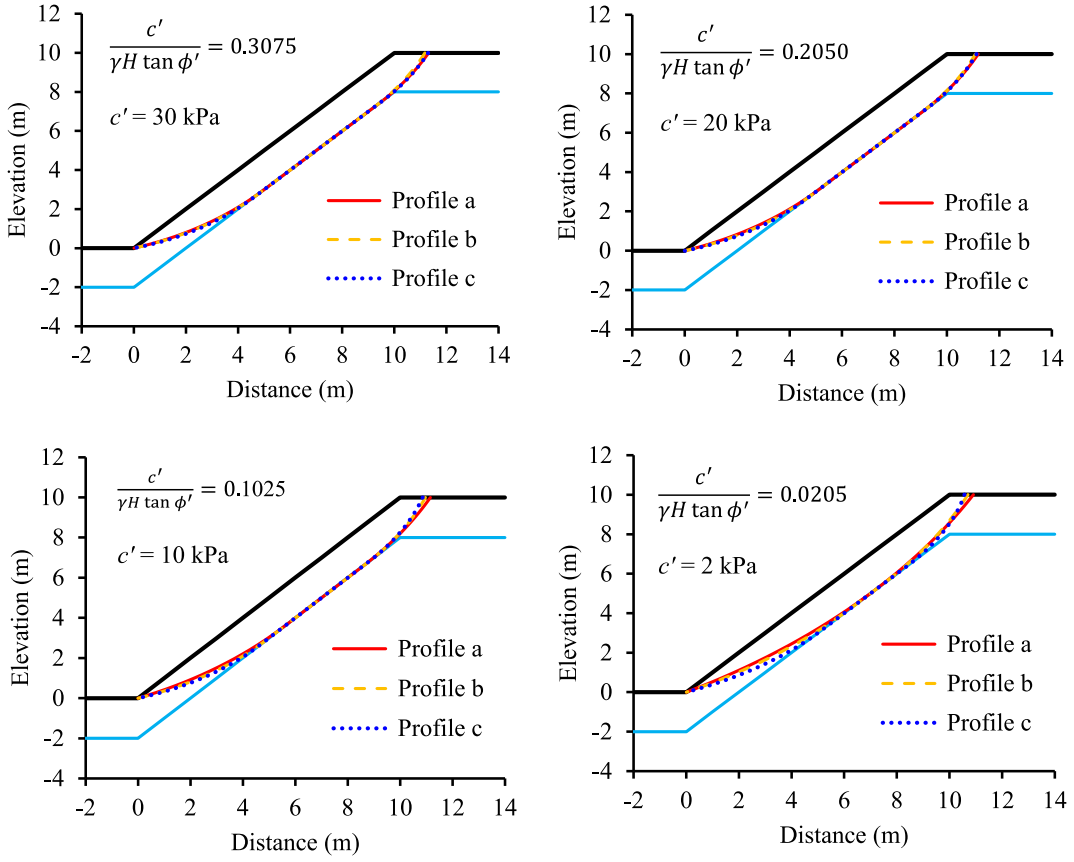

Fig. 7. Influence of pore-water pressure effects on the critical slip surfaces for shallow translational slides (Profile *a* for $u_w < 0$, Profile *b* for $u_w = 0$, and Profile *c* for $u_w > 0$).

portion of the translational component of the slip surface decreases with reduction in $\frac{c'}{\gamma H\tan\phi'}$, and that the translational UBLA reduces to the conventional log-spiral UBLA when $\frac{c'}{\gamma H\tan\phi'} \to 0$. It should be noted that the portion of translational component can also decrease with the increase in $\frac{z_w}{H}$, and that the failure mechanism would generally become purely rotational when $\frac{z_w}{H} > 0.6$ (Huang, 2018).

5. Analytical shallow landslide model accounting for boundary effect

The infinite slope model [Eq. (6)] has been widely used for landslide hazard mapping (e.g., Iverson, 2000; Harp et al. 2006; Baum et al. 2008; Park et al. 2013; Chen & Zhang, 2014) because of its analytical nature. However, the drawback of the infinite slope model is that it neglects boundary effect, and hence, the accuracy is questionable (Taylor, 1948; Griffiths et al. 2011; Milledge et al. 2012; Huang et al. 2015). The commonly used strength reduction finite element method (Griffiths et al. 2011; Milledge et al. 2012; Huang et al. 2015) and the translational UBLA proposed in this study can capture the boundary effect, but they are reserved for site-specific analysis due to the computational expense required. Hence, it is desirable to have an analytical model which retains the simplicity of infinite slope model while accounting for boundary effect. The translational UBLA can be used to develop such an analytical model, as described below.

5.1. Development of the analytical shallow landslide model

A typical stability chart obtained by the translational UBLA presented in Section 2.2 is shown in Fig. 8. The given conditions for the stability chart are $\alpha = 0°$, $\beta = 30°$, $\frac{\gamma_w}{\gamma} = 0.5$, and $\frac{z_w}{H} = 0.2$. For PWP Profile *a*, the additional input parameters are $\frac{\chi h_c}{H} = 0.2$. High linearity is shown between $\frac{F}{\tan\phi'}$ and $\frac{c'}{\gamma H\tan\phi'}$ with coefficients of determination (R^2) greater than 0.999. The correlation between $\frac{F}{\tan\phi'}$ and $\frac{c'}{\gamma H\tan\phi'}$ can be expressed as Eq. (29a), which can be further rearranged as Eq. (29b).

$$\frac{F}{\tan\phi'} = A\frac{c'}{\gamma H\tan\phi'} + B \tag{29a}$$

$$F = A\frac{c'}{\gamma H} + B\tan\phi' \tag{29b}$$

Parameters A and B in Eq. (29) appear as curve-fit parameters, but they have clear physical meanings. As revealed by Eq. (29b), parameters A and B capture the contribution of cohesive resistance and frictional resistance to slope stability, respectively. The former (i.e., parameter A) is affected by boundary effect, and the latter (i.e., parameter B) is independent of boundary effect.

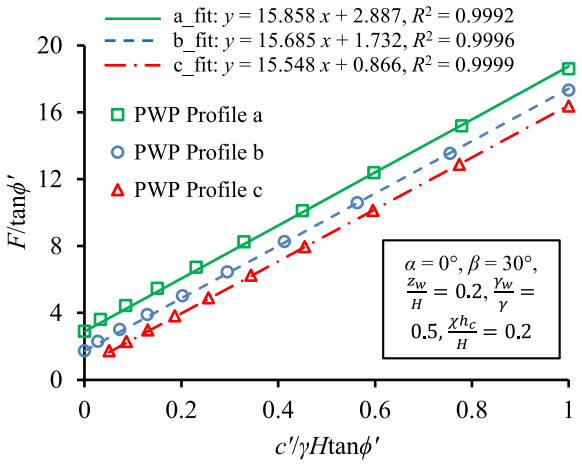

Fig. 8. Stability charts developed by the proposed translational upper bound limit analysis.

When $c' = 0$, Eq. (29b) would be reduced to $F = B\tan\phi'$. The factor of safety F of cohesionless slopes ($c' = 0$) can be calculated exactly by the infinite slope model [Eq. (6)]. Hence, parameter B can be derived analytically as:

$$B = \frac{1}{\tan\beta} - \frac{\chi u_w}{\gamma z_w \sin\beta\cos\beta} \tag{30}$$

Parameter A is affected by boundary effect and can be divided into two components:

$$A = \frac{H}{z_w \sin\beta\cos\beta} + C \tag{31}$$

In the right-hand-side of Eq. (31), the first term captures the contribution of cohesive resistance at the sliding plane where the infinite slope model gives the exact solution, and the second term parameter C captures the contribution of cohesive resistance at the upslope and downslope boundary, which is neglected by the infinite slope model. This point is illustrated more clearly by substituting Eqs. (30) and (31) into Eq. (29b):

$$F = \frac{c'}{\gamma z_w \sin\beta\cos\beta} + \frac{\tan\phi'}{\tan\beta} - \frac{\chi u_w \tan\phi'}{\gamma z_w \sin\beta\cos\beta} + C\frac{c'}{\gamma H} \tag{32}$$

The difference between Eq. (6) and Eq. (32) lies in the last term of Eq. (32) which captures the boundary effect. The boundary effect is quantified by parameter C. A regression model is developed in this study to estimate the parameter C.

The parameters A, B and C for the stability curves in Fig. 8 are summarised in Table 2. For each curve, parameter B is determined by Eq. (30) first. By fitting the curve with Eq. (29a), parameter A is determined using the least square method. Parameter C is then back calculated from Eq. (31).

In this study, stability charts similar to Fig. 8 have been developed for $\beta = \{10°, 15°, \cdots, 70°\}$, and $\frac{z_w}{H} = \{0.02, 0.04, \cdots, 0.30\}$. Hence, a total of 5850 translational UBLAs have been carried out. Parameter C for each set of β and $\frac{z_w}{H}$ is then determined.

For the stability curves presented in Fig. 8, each curve consists of 10 data points. Each data point corresponds to a given ϕ_m', and maximum $\frac{c'}{\gamma H\tan\phi'}$ is determined as discussed in Section 2.2. The value of ϕ_m' can be selected manually. However, manual selection would be tedious for a large number of stability analyses and the data may be skewed if the selection methodology is not systematic. A procedure which enables automatic determination of the ϕ_m' values is outlined below.

1) The $\phi_m^{\max}$ that satisfies the target condition $0 < \frac{c'}{\gamma H\tan\phi'} < 10^{-4}$ is determined. If $\phi_m^{\max} > \beta$ or 45°, $\phi_m^{\max} = \min\{\beta; 45°\}$.
2) The $\phi_m^{\min}$ that satisfies the target condition $\left|\frac{c'}{\gamma H\tan\phi'} - 1\right| < 10^{-4}$ is determined.
3) The i^{th} value ϕ_m^i is exponentially distributed between $\phi_m^{\min}$ and $\phi_m^{\max}$, and calculated by $\phi_m^i = (\phi_m^{\min})^{\frac{i-1}{n-1}} \times (\phi_m^{\max})^{\frac{n-i}{n-1}}$, where n denotes the number of data points on a stability curve (n is taken as 10 in this study), and the value of i ranges from 1 to n.
4) For a specific ϕ_m^i, maximum $\frac{c'}{\gamma H\tan\phi'}$ in Eq. (26b) is determined.

Table 2
Parameters A, B and C for the stability curves in Fig. 8.

Parameter	Profile *a*	Profile *b*	Profile *c*	Calculated by
A	15.858	15.685	15.548	Curve fitting
B	2.887	1.732	0.866	Eq. (30)
C	4.311	4.138	4.001	Eq. (31)

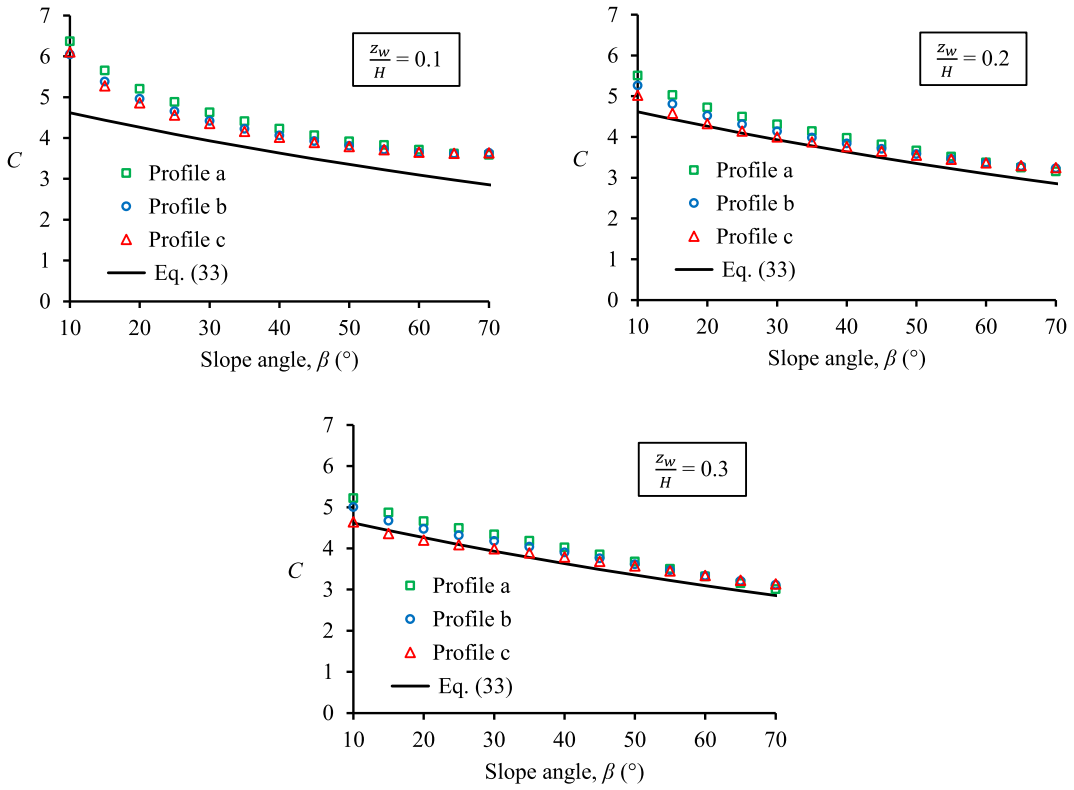

Fig. 9. Parameter C for various pore-water pressure profiles and $\frac{z_w}{H}$.

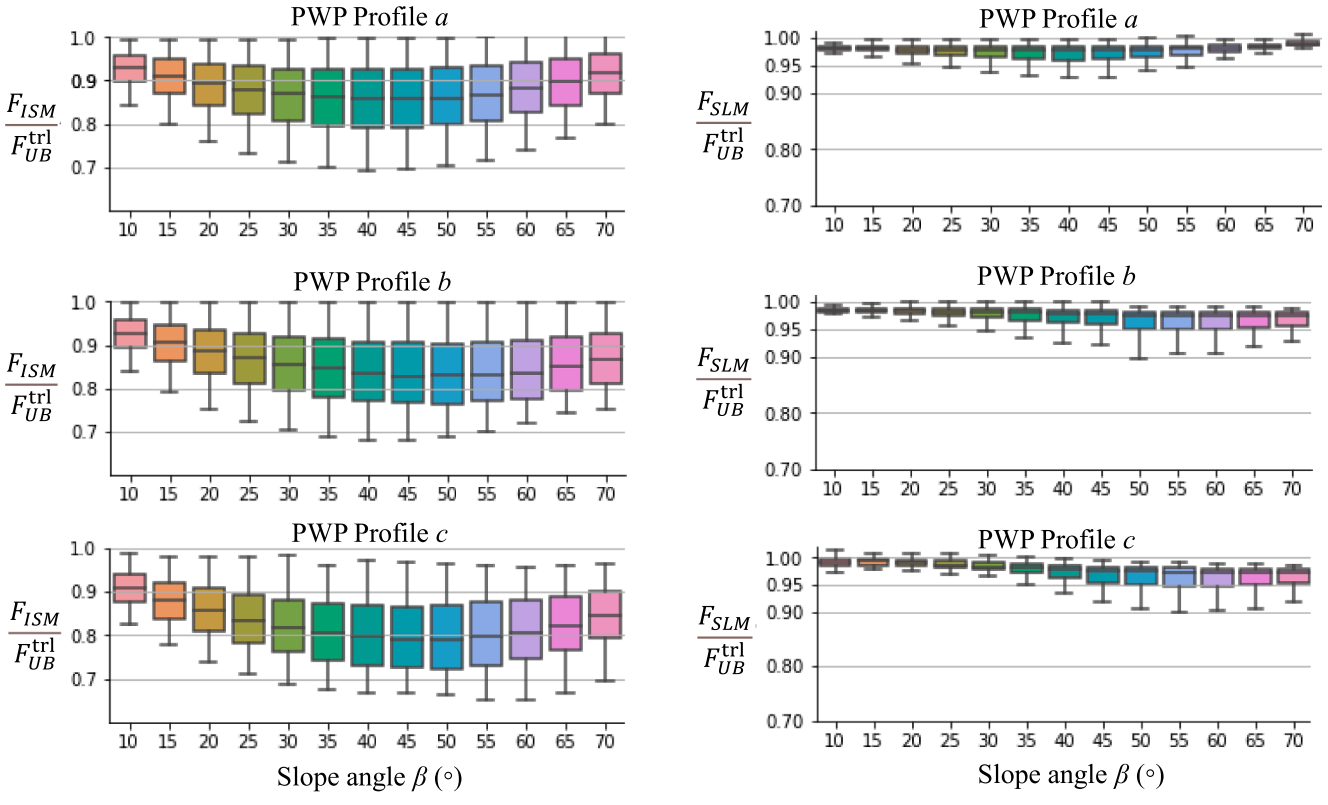

(a) Infinite slope model [Eq. (6)] (b) Shallow landslide model [Eq. (34)]

Fig. 10. Comparisons of factors of safety calculated by the infinite slope model (F_{ISM}) and the proposed shallow landslide model (F_{SLM}) to the translational upper bound solutions (F_{UB}^{trl}) for 5850 case studies ($\frac{z}{H} \leq 0.3$).

By using the above procedure, $\frac{c'}{\gamma H\tan\phi'}$ would range from 0 to 1, as shown in Fig. 8. The value of ϕ'_m distributes exponentially rather than linearly between $\phi_m^{\min}$ and $\phi_m^{\max}$, as the former leads to a more even distribution of data points in the target range of $\frac{c'}{\gamma H\tan\phi'}$ (Huang, 2018). This is important for further curve-fitting and regression analyses.

The parameter C for various β with $\frac{z_w}{H} = 0.1$, 0.2 and 0.3 are shown in Fig. 9. Parameter C is rarely affected by PWP conditions, slightly decreases with increase in $\frac{z_w}{H}$, and is mainly affected by slope angle β. A simple relationship is proposed to approximate parameter C as:

$$C = 5e^{-0.008\beta} \tag{33}$$

Fig. 9 shows that Eq. (33) provides a reasonable lower bound approximation of parameter C for $\frac{z_w}{H} = 0.2$ and 0.3 with all the PWP conditions. For $\frac{z_w}{H} = 0.1$, parameter C is underestimated by Eq. (33), but the error caused on F calculated by Eq. (32) is on the safe side (i.e., underestimated).

Substituting Eq. (33) into Eq. (32), the shallow landslide model can be written as.

$$F = \frac{c'}{\gamma z_w \sin\beta\cos\beta} + \frac{\tan\phi'}{\tan\beta} - \frac{\chi u_w \tan\phi'}{\gamma z_w \sin\beta\cos\beta} + \frac{5c'}{\gamma H}e^{-0.008\beta} \tag{34}$$

It should be noted that in Eqs. (33) and (34) the slope angle β in the exponential function (i.e., $e^{-0.008\beta}$) should be input as degree. The shallow landslide model [Eq. (34)] can be used for both saturated and unsaturated slopes. The effective stress parameter $\chi = 1$ for saturated slopes ($u_w \geq 0$), and $\chi \leq 1$ for unsaturated slopes ($u_w < 0$).

5.2. Accuracy

The accuracy of infinite slope model [Eq. (6)] and the proposed shallow landslide model [Eq. (34)] is comprehensively evaluated here. A total of 5850 translational UBLAs have been carried out to develop the shallow landslide model. The stability solutions are presented in the format of $\frac{F}{\tan\phi'}$ versus $\frac{c'}{\gamma H\tan\phi'}$ (e.g., Fig. 8). For each $\frac{c'}{\gamma H\tan\phi'}$, the $\frac{F}{\tan\phi'}$ from the translational UBLA can be viewed as the exact solution (denoted as $\frac{F_{UB}^{\text{ctrl}}}{\tan\phi'}$). The $\frac{F}{\tan\phi'}$ can also be calculated by the infinite slope model (denoted as $\frac{F_{ISM}}{\tan\phi'}$) and the proposed shallow landslide model (denoted as $\frac{F_{SLM}}{\tan\phi'}$) by rearranging Eq. (6) and Eq. (34) as:

$$\frac{F_{ISM}}{\tan\phi'} = \frac{c'}{\gamma H\tan\phi'}\frac{H}{z_w\sin\beta\cos\beta} + \frac{1}{\tan\beta} - \frac{\chi u_w}{\gamma z_w\sin\beta\cos\beta} \tag{35}$$

$$\frac{F_{SLM}}{\tan\phi'} = \frac{c'}{\gamma H\tan\phi'}\left(\frac{H}{z_w\sin\beta\cos\beta} + 5e^{-0.008\beta}\right) + \frac{1}{\tan\beta} - \frac{\chi u_w}{\gamma z_w\sin\beta\cos\beta} \tag{36}$$

By normalizing the $\frac{F_{ISM}}{\tan\phi'}$ and $\frac{F_{SLM}}{\tan\phi'}$ against $\frac{F_{UB}^{\text{ctrl}}}{\tan\phi'}$, the ratios $\frac{F_{ISM}}{F_{UB}^{\text{ctrl}}}$ and $\frac{F_{SLM}}{F_{UB}^{\text{ctrl}}}$ can be calculated for each case. The ratios are plotted in Fig. 10 as box-and-whisker plots. A box-and-whisker plot shows the minimum value (excluding outliers), 25th percentile, median, 75th percentile, and maximum value (excluding outliers). Fig. 10(a) shows that the ratio $\frac{F_{ISM}}{F_{UB}^{\text{ctrl}}}$ is generally between 0.75 and 0.9, which means that the infinite slope model could underestimate the slope stability by 10%~25%. Fig. 10(b) shows that the ratio $\frac{F_{SLM}}{F_{UB}^{\text{ctrl}}}$ is generally between 0.95 and 1. This means that by introducing the correction term to account for the boundary effects, the proposed shallow landslide model significantly improve the accuracy with error generally less than 5% (slightly conservative estimate).

The accuracy of the infinite slope model and the proposed shallow landslide model is further evaluated with the finite element lower bound and upper bound solutions presented in Table 1. The results are plotted in Fig. 11. Infinite slope model can underestimate the factor of safety by about 20%. The factors of safety predicted by the proposed shallow landslide model agree well with the finite element lower bound and

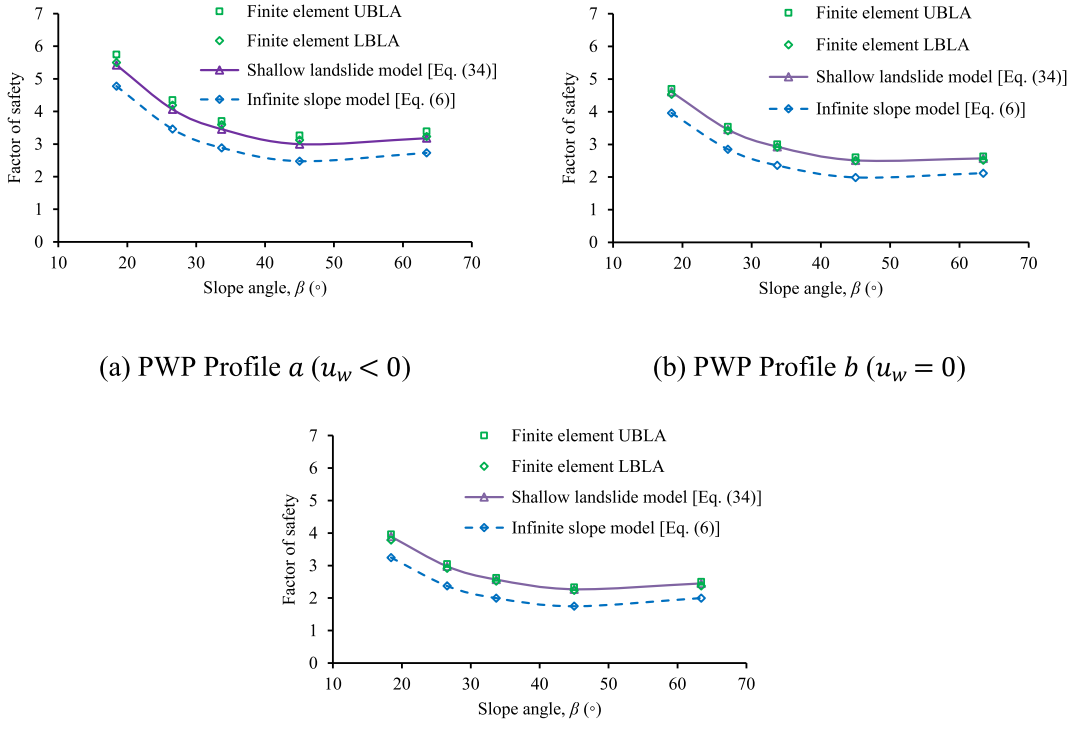

Fig. 11. Comparison of factors of safety obtained by finite element lower and upper bound limit analyses, infinite slope model and the proposed shallow landslide model ($c' = 30$ kPa, $\phi' = 26°$, $\gamma = 20$ kN/m^3, $H = 10$ m, $z_w = 2$ m).

upper bound solutions with differences generally less than 2%.

6. Conclusions

Rainfall is one of the common factors that triggers landslides. Due to rainfall infiltration, suction can be partially eliminated, completely eliminated or positive pore-water pressures can be built up above the wetting front. This study has presented a rigorous upper bound limit analysis (UBLA) of shallow landslides with an innovative kinematically admissible hybrid translational failure mechanism and systematic consideration of pore-water pressure effects. A database of 5850 slope cases analysed using the translational UBLAs were then used to develop a new analytical shallow landslide model accounting for boundary effects. The main conclusions from this study are:

- The proposed translational UBLA was validated by finite element limit analyses (both lower bound and upper bound). The critical slip surface predicted by the translational UBLA was found to be in good agreement with finite element limit analyses, and much more appropriate than the conventional log-spiral failure mechanism. The latter was shown to underpredict the failure volume and overpredict the factor of safety.
- The location of the critical slip surface and hence contribution of the boundary effect to shallow slope stability are rarely affected by pore-water pressure conditions, hence confirming that location is mainly determined by $\frac{c'}{\gamma H\tan\phi'}$. The increase of factor of safety due to the boundary effect can be approximated as $\frac{5c'}{\gamma H}e^{-0.008\beta}$.
- The proposed new analytical shallow landslide model [Eq. (34)] is shown to have accuracy within 5% for the 5850 cases considered. This is an improvement on the conventional infinite slope model [Eq. (6)], which may underestimate the factor of safety by 10% to 25%.
- Consequently, the analytical shallow landslide model offers a simple way to carry out regional slope stability analysis or landslide hazard mapping covering large volumes of slopes, with little loss in accuracy and exceptionally low computational expense.

CRediT authorship contribution statement

Wengui Huang: Conceptualization, Data curation, Formal analysis, Investigation, Methodology, Project administration, Software, Validation, Visualization, Writing – original draft, Writing – review & editing. **Fleur Loveridge:** Funding acquisition, Supervision, Writing – review & editing. **Alfrendo Satyanaga:** Writing – review & editing.

Declaration of Competing Interest

The authors declare that they have no known competing financial interests or personal relationships that could have appeared to influence the work reported in this paper.

Data Availability

All data, models, or code that support the findings of this study are available from the corresponding author upon reasonable request.

Acknowledgements

The work is supported by programme grant ACHILLES (grant number EP/R034575/1) funded by the UK Engineering and Physical Sciences Research Council (EPSRC). Professor Vaughan Griffiths kindly provided helpful comments on an earlier draft of this paper.

Appendix

The work rate balance equation for Profile b is given by Eq. (9). The coefficients used to calculate each component of the work rate balance equation are provided below.

The coefficients f_1, f_2 and f_3 used to calculate the rate of work done by weight of the rotational mass, i.e. Eq. (10), are given below.

$$f_1=\frac{1}{3\left[1+9(\tan\phi')^2\right]}\left\{(3\tan\phi'\cos\theta_h+\sin\theta_h)e^{3(\theta_h-\theta_o)\tan\phi'}-(3\tan\phi'\cos\theta_o+\sin\theta_o)\right\} \tag{A1}$$

$$f_2=\frac{1}{6}\frac{L}{r_o}\left(2\cos\theta_o-\frac{L_{AB}}{r_o}\cos\alpha\right)\sin(\theta_o+\alpha) \tag{A2}$$

$$f_3=\frac{1}{6}e^{(\theta_h-\theta_o)\tan\phi'}\left[\sin(\theta_h-\theta_o)-\frac{L_{AB}}{r_o}\sin(\theta_h+\alpha)\right]\left[e^{(\theta_h-\theta_o)\tan\phi'}\cos\theta_h+\cos\theta_o-\frac{L_{AB}}{r_o}\cos\alpha\right] \tag{A3}$$

The $\frac{L_{AB}}{r_o}$ in Eq. (A2) and Eq. (A3) can be calculated by.

$$\frac{L_{AB}}{r_o}=\frac{\sin(\beta+\theta_o)}{\sin(\beta-\alpha)}-\frac{\sin(\beta+\theta_h)}{\sin(\beta-\alpha)}e^{(\theta_h-\theta_o)\tan\phi'} \tag{A4}$$

From Eq. (A2) to Eq. (A4), α is the angle at slope crest, β is the slope angle, and L_{AB} is the length at slope crest insersected by the slip surface, as shown in Fig. 3.

The coefficient f_γ^{trl} used to calculate the rate of work done by weight of the translational mass, i.e. Eq. (11), is.

$$f_\gamma^{\mathrm{trl}}=\frac{H_{\mathrm{trl}}}{r_o}\frac{z_s}{r_o}\left[e^{(\theta_z-\theta_o)\tan\phi'}-\frac{z_s\cos\beta}{2r_o\cos\phi'}\right]\frac{\cos\theta_z}{\tan\beta} \tag{A5}$$

where $\frac{z_s}{r_o}$ and θ_z can be calculated by Eq. (24) and Eq. (25), respectively.

The coefficient $f_{c'}^{\mathrm{rot}}$ used to calculate energy dissipation caused by the rotational mass, i.e. Eq. (12), is.

$$f_{c'}^{\mathrm{rot}}=\frac{1}{2}\frac{H}{r_o}\left[e^{2(\theta_h-\theta_o)\tan\phi'}-1\right] \tag{A6}$$

The coefficient $f_{c'}^{\mathrm{trl}}$ used to calculate energy dissipation caused by the translational mass, i.e. Eq. (13), is.

$$f_{c'}^{\mathrm{trl}} = \frac{H}{r_o}\frac{H_{\mathrm{trl}}}{r_o}e^{(\theta_z-\theta_o)\tan\phi'}\frac{\sin\phi'}{\sin\beta} \tag{A7}$$

References

Atkinson, J., 2007. The mechanics of soils and foundations, 2nd ed. Taylor & Francis.

Baum, R.L., Savage, W.Z., Godt, J.W., 2008. TRIGRS-A Fortran program for transient rainfall infiltration and grid-based regional slope-stability analysis, version 2.0. US Geological Survey Open-File Report 2008–1159.

Bishop, A.W., Blight, G.E., 1963. Some aspects of effective stress in saturated and partly saturated soils. Géotechnique 13 (3), 177–197. https://doi.org/10.1680/geot.1963.13.3.177.

Chen, H.X., Zhang, L.M., 2014. A physically-based distributed cell model for predicting regional rainfall-induced shallow slope failures. Eng. Geol. 176, 79–92. https://doi.org/10.1016/j.enggeo.2014.04.011.

Chen, W.F., 1975. Limit Analysis and Soil Plasticity. Elsevier Science, Amsterdam, the Netherlands.

Cho, S.E., 2009. Infiltration analysis to evaluate the surficial stability of two-layered slopes considering rainfall characteristics. Eng. Geol. 105 (1–2), 32–43. https://doi.org/10.1016/j.enggeo.2008.12.007.

Dahal, R.K., Hasegawa, S., Nonomura, A., Yamanaka, M., Masuda, T., Nishino, K., 2009. Failure characteristics of rainfall-induced shallow landslides in granitic terrains of Shikoku Island of Japan. Eng. Geol. 56 (7), 1295–1310. https://doi.org/10.1007/s00254-008-1228-x.

Dai, F.C., Lee, C.F., Wang, S.J., 2003. Characterization of rainfall-induced landslides. Int. J. Remote Sens. 24 (23), 4817–4834. https://doi.org/10.1080/01431160131000082424.

Davis, R.O., Selvadurai, A.P.S. (Eds.), 2002. Plasticity and Geomechanics. Cambridge University Press.

Fredlund, D.G., Rahardjo, H., 1993. Soil mechanics for unsaturated soils. John Wiley & Sons.

Griffiths, D.V., Huang, J., Dewolfe, G.F., 2011. Numerical and analytical observations on long and infinite slopes. Int. J. Numer. Anal. Methods Geomech. 35 (5), 569–585. https://doi.org/10.1002/nag.909.

Harp, E.L., Michael, J.A., Laprade, W.T., 2006. Shallow-Landslide Hazard Map of Seattle, Washington. US Geological Survey Open-File Report 2006–11139.

Huang, W., 2021. Efficient analytical approach for stability analysis of infrastructure slopes. Proc. Inst. Civ. Eng.: Geotech. Eng. 1–14 https://doi.org/10.1680/jgeen.21.00106.

Huang, W., 2018. Stability of unsaturated soil slopes under rainfall and seismic loading. Nanyang Technological University, Singapore. PhD thesis.

Huang, W., Leong, E.C., Rahardjo, H., 2015. Translational slip failures on slope incorporating unsaturated soil mechanics. In: Proc 6th Asia-Pacific Conf. on Unsaturated Soil, 23rd – 26th, October 2015, Guilin, China, pp. 771–775.

Huang, W., Leong, E.C., Rahardjo, H., 2016. Governing failure mode of unsaturated soil slopes under rainfall infiltration. In: 3rd European Conf. on Unsaturated Soils, 12th – 14th September, 2016, Paris, France. https://doi.org/10.1051/e3sconf/20160915008.

Huang, W., Leong, E.C., Rahardjo, H., 2018. Upper-bound limit analysis of unsaturated soil slopes under rainfall. J. Geotech. Geoenviron. Eng. 144 (9), 04018066. https://doi.org/10.1061/(ASCE)GT.1943-5606.0001946.

Iverson, R.M., 2000. Landslide triggering by rain infiltration. Water Resour. Res. 36 (7), 1897–1910. https://doi.org/10.1029/2000WR900090.

Ji, J., Wang, C.W., Gao, Y., Zhang, L., 2021. Probabilistic investigation of the seismic displacement of earth slopes under stochastic ground motion: A rotational sliding block analysis. Can. Geotech. J. 58 (7), 952–968. https://doi.org/10.1139/cgj-2020-0252.

Jiang, J.C., Yamagami, T., 2006. Charts for estimating strength parameters from slips in homogeneous slopes. Comput. Geotech. 33 (6–7), 294–304. https://doi.org/10.1016/j.compgeo.2006.07.005.

Kayyal, M.K., Wright, S.G., 1991. Investigation of long-term strength properties of Paris and Beaumont clays in earth embankments. Research Report 1195-2F, Center for Transportation Research, University of Texas at Austin, Austin, Texas.

Krabbenhoft, K., 2019. OptumG2: Theory, Optum Computational Engineering. Available at www.optumce.com.

Lee, L.M., Gofar, N., Rahardjo, H., 2009. A simple model for preliminary evaluation of rainfall-induced slope instability. Eng. Geol. 108 (3–4), 272–285. https://doi.org/10.1016/j.enggeo.2009.06.011.

Lian, J., Wu, J., 2021. Surficial stability analysis of soil slope under seepage based on a novel failure mode. Front. Struct. Civ. Eng. 15 (3), 712–726.

Michalowski, R.L., 1995. Slope stability analysis: a kinematical approach. Géotechnique 45 (2), 283–293. https://doi.org/10.1680/geot.1995.45.2.283.

Milledge, D.G., Griffiths, D.V., Lane, S.N., Warburton, J., 2012. Limits on the validity of infinite length assumptions for modelling shallow landslides. Earth Surf. Process. Landf. 37 (11), 1158–1166. https://doi.org/10.1002/esp.3235.

Nuth, M., Laloui, L., 2008. Effective stress concept in unsaturated soils: Clarification and validation of a unified framework. Int. J. Numer. Anal. Methods Geomech. 32 (7), 771–801. https://doi.org/10.1002/nag.645.

Park, H.J., Lee, J.H., Woo, I.K., 2013. Assessment of rainfall-induced shallow landslide susceptibility using a GIS-based probabilistic approach. Eng. Geol. 161, 1–15. https://doi.org/10.1016/j.enggeo.2013.04.011.

Perry, J., 1989. A survey of slope condition on motorway earthworks in England and Wales. Research Report 199. Transport & Road Research Laboratory, Crowthorne.

Qin, C., Chian, S.C., 2018. Bearing capacity analysis of a saturated non-uniform soil slope with discretization-based kinematic analysis. Comput. Geotech. 96, 246–257.

Rahardjo, H., Lim, T.T., Chang, M.F., Fredlund, D.G., 1995. Shear-strength characteristics of a residual soil. Can. Geotech. J. 32 (1), 60–77. https://doi.org/10.1139/t95-005.

Sloan, S.W., 2013. Geotechnical stability analysis. Géotechnique 63 (7), 531–571.

Smethurst, J.A., Clarke, D., Powrie, W., 2012. Factors controlling the seasonal variation in soil water content and PWPs within a lightly vegetated clay slope. Géotechnique 62 (5), 429–446. https://doi.org/10.1680/geot.10.P.097.

Taylor, D.W., 1948. Fundamentals of Soil Mechanics. Soil Sci. 66 (2), 161.

Yu, H.S., Salgado, R., Sloan, S.W., Kim, J.M., 1998. Limit analysis versus limit equilibrium for slope stability. J. Geotech. Geoenviron. Eng. 124 (1), 1–11. https://doi.org/10.1061/(ASCE)1090-0241(1998)124:1(1).

Zhang, L.L., Fredlund, D.G., Zhang, L.M., Tang, W.H., 2004. Numerical study of soil conditions under which matric suction can be maintained. Can. Geotech. J. 41 (4), 569–582. https://doi.org/10.1139/t04-006.

Zhan, T.L., Ng, C.W., Fredlund, D.G., 2007. Field study of rainfall infiltration into a grassed unsaturated expansive soil slope. Can. Geotech. J. 44 (4), 392–408. https://doi.org/10.1139/t07-001.